Advances in Aircraft and Spacecraft Science, *Vol. 9, No. 1 (2022) 1-15*
https://doi.org/10.12989/aas.2022.9.1.001

Calibration of flush air data sensing systems for a satellite launch vehicle

R.C. Mehta*

Department of Aeronautical Engineering, Noorul Islam Centre for Higher Education, Kumaracoil 629180, India

(Received June 25, 2021, Revised October 23, 2021, Accepted December 10, 2021)

Abstract. This paper presents calibration of flush air data sensing systems during ascent period of a satellite launch vehicle. Aerodynamic results are numerically computed by solving three-dimensional time dependent compressible Euler equations over a payload shroud of a satellite launch vehicle. The flush air data system consists of four pressure ports flushed on a blunt-cone section of the payload shroud and connected to on board differential pressure transducers. The inverse algorithm uses calibration charts which are based on computed and measured data. A controlled random search method coupled with neural network technique is employed to estimate pitch and yaw angles from measured transient differential pressure history. The algorithm predicts the flow direction stepwise with the function of flight Mach numbers and can be termed as an online method. Flow direction of the launch vehicle is compared with the reconstructed trajectory data. The estimated values of the flow direction are in good agreement with them.

Keywords: glass structures; impact load; pendulum test

1. Introduction

Angle of attack (AoA) of a satellite launch vehicle is important parameters to assess the health, aerodynamic performance and behaviour of the launch vehicle during transonic speed and maximum dynamic pressure regime. Using angle of attack data, instantaneous structural loads, wind and effects of transonic buffeting can be checked and verified with the aerodynamic design as well as expansion of the flight envelope. It is proposed here to use an flush air data sensing system (FADS) to measure pitch angle and side-slip angle along with other basic aerodynamic parameters such as Mach number, dynamic, static and stagnation pressure, throughout transonic to supersonic Mach numbers range. The satellite launch vehicle loads are the greatest in the transonic flight regime.

Estimation of AoA is an essential aerodynamic quantity in the post-flight analysis (PFA) reconciliation of flight measurement data with ground based wind-tunnel experiments and computational fluid dynamics (CFD) simulations. On board inertial measurement units (IMU) are used to compute vehicle velocity with respect to a fixed coordinate system in conjunction with trajectory of the vehicle. The determination of air data is a technique based on flowfield pressure measurement consisting of a number of pressure tapings flush with the vehicle surface, usually in

*Corresponding author, Professor, E-mail: drrakhab.mehta@gmail.com

http://www.techno-press.org/?journal=aas&subpage=7 ISSN: 2287-528X (Print), 2287-5271 (Online)

the blunt-nose section of the payload shroud. The measured distribution of the pressure field around the nose is then used to infer the air data. A minimum of four pressure ports are required to obtain a complete set of air data parameters.

A method for the determination of air data is a technique based on flowfield pressure measurement because FADS is sensitive to pressure port location. Different types of air data systems are available such as fuselage body pressure mounting probes and blunt forebody attaching with an aerospike. The difference of measured pressure on the wedge or cone surfaces (Liepmann *et al*. 2007) can be related to flow conditions by employing oblique shock relations and conical shock charts, respectively. Larson *et al*. (1990) employed wind tunnel data to study FADS performance of vehicles at Mach numbers from 0.7 to 1.4. They evaluated freestream values of stagnation pressure, static pressure, Mach number and AoA from FADS. An aerospike is employed on the external tank of the space shuttle to measure AoA during the ascent phase of the flight (Hillje *et al*. 1993). In the PFA the measured pressure obtained through the telemetry is used to estimate angle of attack and sideslip angle in conjunction with wind tunnel data.

Aerodynamic characteristics of high speed vehicles are evaluated employing flight data by Watanbe *et al*. (1997). Design and calibration of FADS of the X-33 has been performed by Whitmore *et al*. (1998). Neural networks have been developed (Rohloff *et al*. 1998) to estimate freestream static and dynamic pressures from an array of pressure measurements taken from ports located flush on the nose of an aircraft. Cobleigh *et al*. (1999) calibrated FADS pressure model and solution algorithm of a sphere, spherical cones, a Rankine half-body, and the F-14, F/A-18, X-33, X-34, and X-38 configurations. Johnson *et al*. (1999) have conducted experimental and numerical simulation of flow field over a forebody of HYFLEX vehicle. It has been concluded by them that CFD provides a quick and inexpensive way to calibrate the air data system and is applicable to a broad range of flight conditions. FADS on a sharped-nosed body for Mach 3 to 8 has been developed by Davis *et al*. (2000). Fan *et al*. (2003) used neural network based calibration techniques to evaluate aerodynamics of multi-hole pressure probes. Rohlf *et al*. (2004) carried out vector identification of X-31using FADS. Neural network based flush air data system has been applied on a mini air vehicle by Samy *et al*. (2010). They found that the CFD simulations are useful to identify the ideal pressure port locations. Baumann *et al*. (2010) applied FADS to analyze test results of X-43A. Paces *et al*. (2010) analyzed angle of attack and sideslip angle using twin differential sensor modules. FADS have been applied to evaluate the performance of UAV by Quindlen *et al*. (2013). Comparative study on solving various flush air data systems has been presented by Liu *et al*. (2014). Chen *et al*. (2015) studied the FADS of hypersonic vehicles using an algorithm based on neural networks. Srivastava and Meade (2015) carried out a comprehensive probabilistic framework to learn air data from surface pressure measurements. Karlguard *et al*. (2017) coupled inertial navigation and FADS algorithm for estimation atmospheric estimation. Shevchenko and Shmakov (2017) have evaluated multi-hole probes in wind-tunnel experiments in conjunction with FADS. Reis *et al*. (2019) applied optimization of aerodynamics for airfoil inverse design. It shows that a large number of research papers have appeared for analysis of flow using FADS in conjunction with neural network algorithms. The calibration requires a large database to train a multi-layer neural network to predict the aerodynamic characteristics of a vehicle.

Correction factors may be obtained from wind-tunnel tests but these may not cover the entire flight envelope. Using a validated CFD flow solver to generate a suite of correction factors is an attractive option due to its wide range of applicability, low cost, and very high precision. Anderson *et al*. (1986) have used finite volume flux splitting method to solve compressible Euler equations. Computed results of inviscid flow field around aerospace vehicles have been compared with

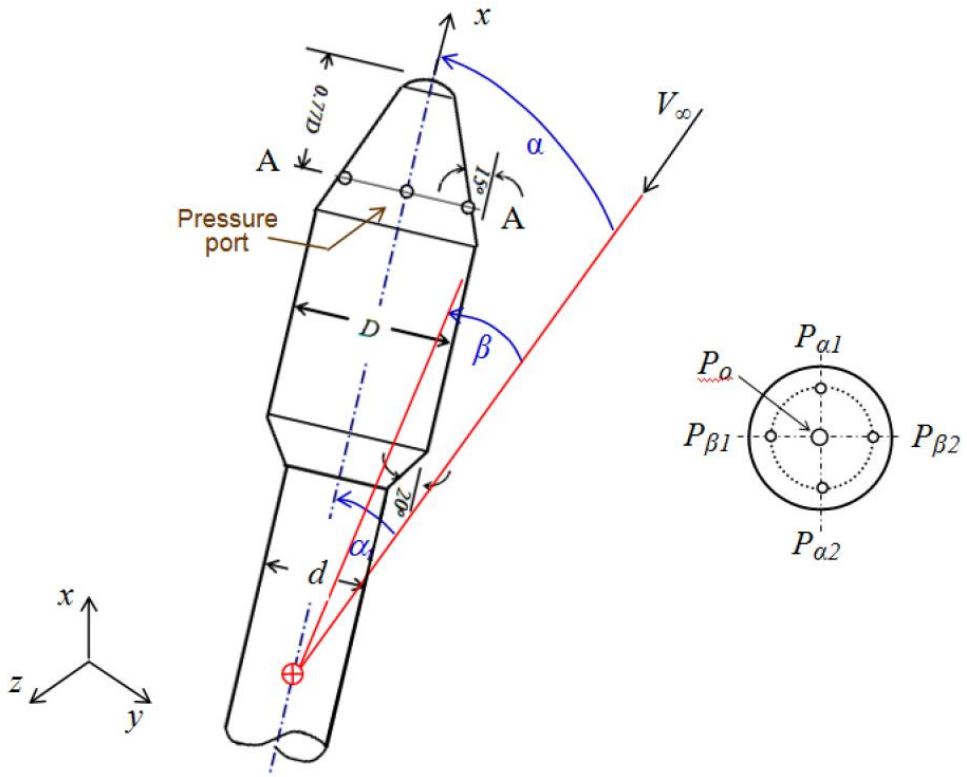

Fig. 1 (a) Schematic sketch of a satellite launch vehicle (b) section A-A at x/D=0.77

experimental and flight data by An *et al*. (1993). Literature survey reveals that the three-dimensional compressible Euler equations are used to compute flowfield over launch vehicles. Their prediction of aerodynamic characteristics based on wind-tunnel test results and numerical data are employed for Mach numbers from 2 to 14.

In this paper, a study of inverse analysis using controlled random search (CRS) algorithm in conjunction with neural network method is applied to estimate pitch angle α, sideslip angle β and AoA α_t for a freestream velocity vector V_∞ of a typical satellite launch vehicle as depicted in Fig. 1 (a). Pressure ports are located x/D=0.77. Locations of pressure ports are shown in Fig. 1(b). The three-dimensional Euler equations are used for computation of pressure distribution for freestream Mach numbers range 0.5 to 3.0 and at angles of attack ±5º. Measured differential Pressure data was converted to the desired air data through a calibration data curve employing CRS method in conjunction with neural network technique.

2. Numerical analysis

2.1 Governing equations

The normal pressure across the blunt-cone section of the payload fairing is negligible and because there is no boundary layer separation in this region. The fluid motion is governed by time

dependent three-dimensional compressible inviscid equations for the ideal and perfect gas which express the conservation of mass, momentum and energy in the absence of external forces. The Cartesian coordinate form of the Euler equations can be expressed as

$$\frac{\partial \boldsymbol{U}}{\partial t}+\frac{\partial \boldsymbol{E}}{\partial x}+\frac{\partial \boldsymbol{F}}{\partial y}+\frac{\partial \boldsymbol{G}}{\partial z}=0 \tag{1}$$

where $\boldsymbol{U}$ is vector of conserved quantities and is written as

$$\boldsymbol{U}=\left[\rho,\rho u,\rho v,\rho w,\rho e\right]^{T} \tag{2}$$

where u, v, and w are the velocities in the x, y, and z directions, respectively. $\boldsymbol{F}$, $\boldsymbol{G}$ and $\boldsymbol{H}$ are Cartesian inviscid flux vectors. The inviscid flux vectors will not be repeated here but can be found in the texts by (Bertin 2006). Temperature is related to the perfect gas equation of state. The ratio of specific heats was assumed constant and taken equal to 1.4.

2.2 Solution procedure

To simplify the spatial discretization in numerical simulations, Eq. (1) can be written in the integral form over a finite computational domain with the boundary as

$$\int_{\Omega}\boldsymbol{U}d\Omega+\int_{\Gamma}\left(\boldsymbol{E}+\boldsymbol{F}+\boldsymbol{G}\right)d\Gamma=0 \tag{3}$$

Here Ω is a control volume with surface Γ. The contour integration around the boundary of the cell is performed in an anticlockwise sense in order to keep flux vectors normal to the boundary of the cell. The computational domain has a finite number of non-overlapping hexahedral cells. In a cell centred finite volume method, the flux variables are stored at the centroid of the grid cell and the control volume is formed by the cell itself. The conservation variables within the computational cell are represented by their average values at the cell centre.

The inviscid fluxes are computed at the cell-centre resulting in flux balance. The summation is carried out over the eight edges of the cell. The space discretization scheme shares the reconstruction of the conservative variables of cell interfaces but differs in the evaluation of fluxes in time stepping. The inviscid fluxes are obtained from Roe's approximate Reimann solver. The numerical scheme is advanced in time with a third order Runge-Kutta method. AUSM+ scheme (Liou 2006) is employed here to evaluate the inviscid fluxes by splitting them as convective and pressure terms. The spatial discretization described above reduces the integral equation to semi-discrete ordinary differential equations. The numerical algorithm is second-order accurate in space discretization and time integration. The numerical scheme is stable for a Courant number ≤ 2. Local time steps are used to accelerate to a steady-state solution by setting the time-step at each point to the maximum value allowed by the local Courant-Friedrichs-Lewy (CFL) condition.

2.3 Initial and boundary conditions

To solve Eq. (1), one has to have the initial boundary conditions, which defines a particular problem. At the inflow, all the flow variables are taken at the freestream values as tabulated (Mehta 2017a) including flight trajectory (Mehta 2017b).

At a solid wall, the velocity tangential to the boundary is applied since the flow is inviscid. At

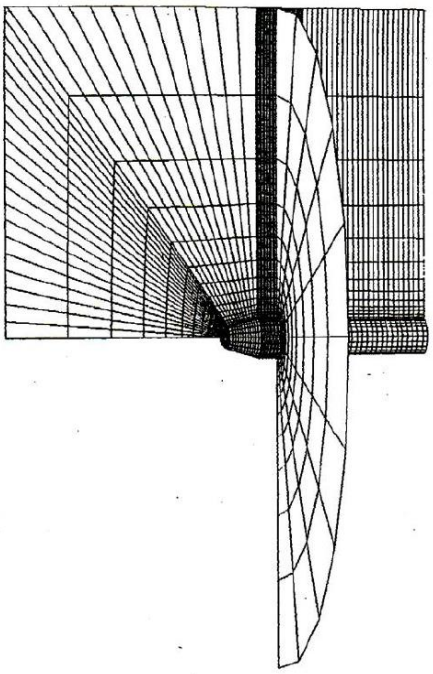

Fig. 2 Computational grid over the satellite launch vehicle

transonic freestream Mach number, the computational domain of dependence is unbounded, and the implementation of boundary and initial conditions become critical, the known physical acceptance of far-field boundary conditions usually limit the flow variables to asymptotic values at large distances from the payload fairing. Therefore, suitable coordinate stretching and placement of the far-field boundary condition have been considered in numerical simulations. The freestream conditions are prescribed on the outer boundary. For supersonic flow, all of the flow variables are extrapolated from the vector of conserved variables $\boldsymbol{U}$. An image cell is imposed to the solved variables at the line of symmetry ahead of the vehicle.

2.4 Payload fairing geometry and pressure ports

The maximum diameter of the payload shroud is D=35 mm and the booster diameter is d=8.75 mm. The spherical cap of the payload fairing is R_N=8.75 mm. For the blunt-nosed cone, the inclination at the fore body is 20º. The boat tail angle is measured clockwise from the axis with reference to the oncoming flow direction and is 15º. The location of the pressure ports are $P_{\alpha 1}$, $P_{\alpha 2}$, $P_{\beta 1}$ and $P_{\beta 2}$ flush mounted pressure transducers at x=0.77D. Fig. 1 depicts the nomenclature of pressure ports.

2.5 Computational grid

The body-oriented grids are generated using a one-to-one and onto method in conjunction with finite element method (Mehta 2017c) to obtain stretched and non-overlapping grid in a single block of the payload fairing. The stretched grids are generated in an orderly manner. The mesh is

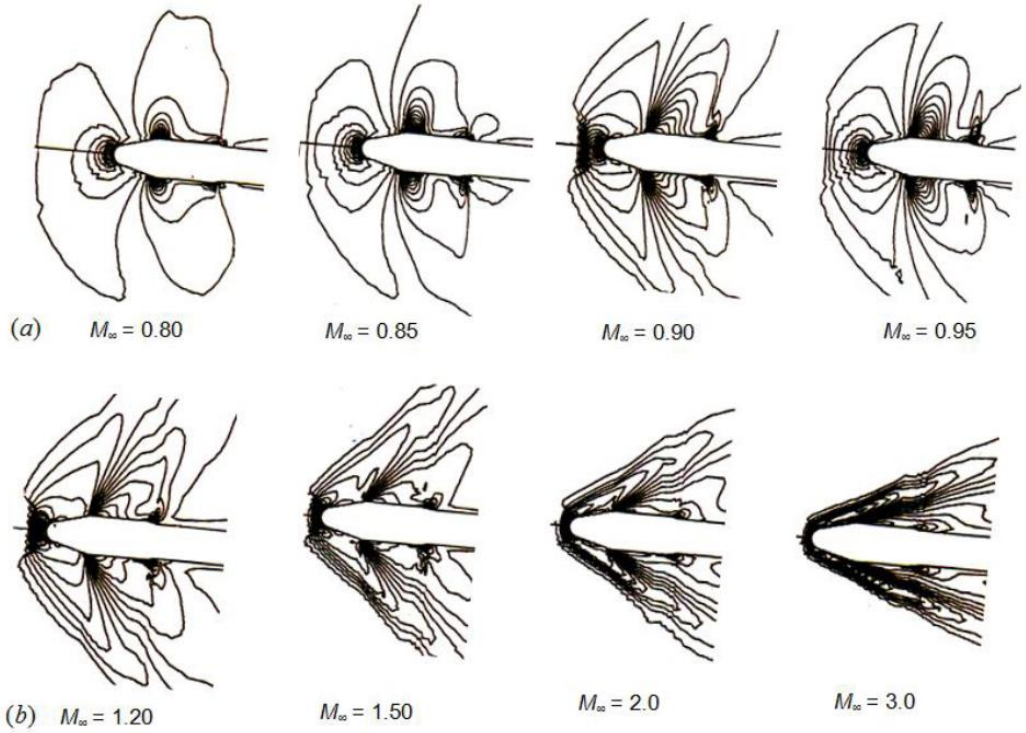

Fig. 3 Density contours (a) transonic (b) supersonic Mach numbers

exponentially stretched from the wall. The grid-stretching factor is selected as 4, and the outer boundary of the computational domain is maintained as 3.5-4.5 times maximum diameter *D*. In the downstream direction, the computational boundary is about 6-9 times the diameter *D*. The computational domain depends on freestream Mach number. The internal grid cells were constructed so that all of the nose pressure ports coincide with the centre of a finite volume cell face. The computational grid is shown in Fig. 2 and has 110 planes axially, 26 planes circumferentially, and 70 planes normal to the body. The grid arrangement is found to yield a relative difference of about ±3% in the pressure peak, which is in the same range as the stagnation pressure measurement error in the wind-tunnel. The convergence criterion is based on the difference in density values at any of the grid points, between two successive iterations $|\rho^{n+1}-\rho^{n}|\leq 10^{-5}$ where n is time-step counter. The numerical computations were carried out with various grid arrangements in order to meet a grid independency check. The minimum grid size in the normal direction of the payload fairing is about 1.70×10^{-4} of nose radius R_N.

2.6 Flowfield characteristics

The three-dimensional Euler code was developed by us and used to simulate flow over the payload fairing. The code is second-order time accurate; the flow around the payload fairing is instantaneously steady at all points in flight. The assumption is reasonable, since only small changes in flow conditions occur over the time required for full development of the flowfield. It is important to mention here that the assumption allows the generation of CFD flow solutions at any

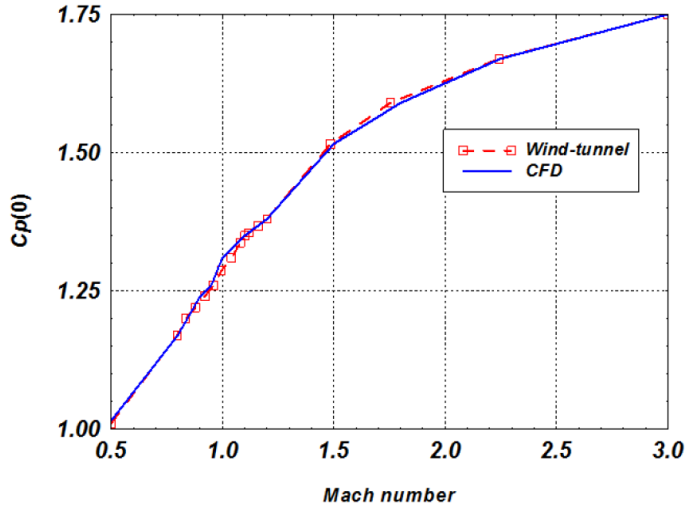

Fig. 4 Variation of stagnation pressure coefficient

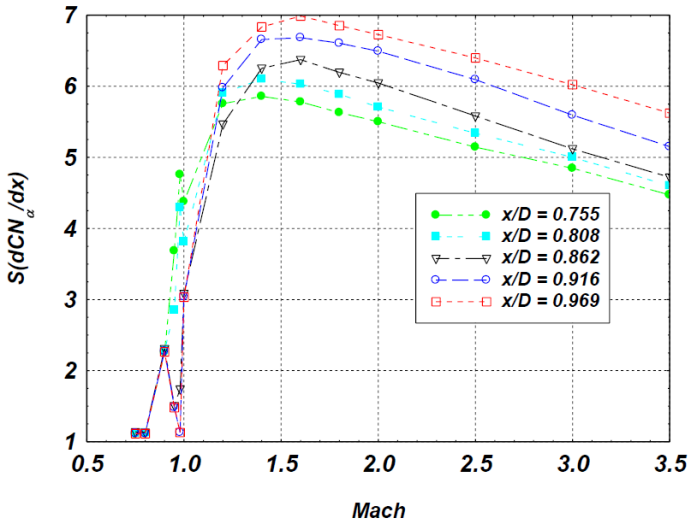

Fig. 5 Normal load in blunt-cone section of payload fairing

point on the trajectory, independent of previous flight conditions. Simulations of the flowfield over the payload fairing were performed at various AoA and flight conditions.

The numerical procedure produced results of comparable accuracy to that obtained by wind tunnel data. The wind-tunnel tests were carried out on a 1/120 scale model of the full-size launch vehicle at up to angle of attack of ±5º with an interval of 1º. The subscale dimension of the scale model is selected after considering the blockage and compatibility conditions with the model support system of the wind tunnel.

Numerical simulations are carried out for flight Mach numbers of 0.5 to 3.0 at an increment of angle of attack $\Delta\alpha$=0.25º. Fig. 3 shows the density contours at various M_∞ at AoA=±5º. Fig. 3 shows the density contours in the plane of symmetry. It can be seen from the density contours that the flowfield characteristics depend on flight Mach numbers. The density contours in Fig. 3(a)

exhibits the transonic flow behaviour of flowfield over the payload fairing. The terminal shock moves downstream on the payload fairing for M_∞<1. Fig. 3(b) shows formation of bow shock over the forebody and presence of weak oblique shocks downstream of the cone-cylinder junction of the payload fairing for M_∞>1. The difference in the shock shapes significantly affected the surface pressure distributions. The expansion and compression on the shoulder points of the payload fairing are visible in the density contours.

The pressure coefficient $Cp(0)=[(p_o-p_\infty)/q_\infty]$ at the stagnation point is shown in Fig. 4 where p_o is the stagnation pressure, p_∞ is freestream pressure and q_∞ is freestream dynamic pressure. Stagnation point pressure coefficient is compared with wind tunnel results. The stagnation pressure coefficients can also be obtained using the analytically isentropic equations (Liepmann *et al*. 2007) as

$$Cp(0)=\left[1+\frac{\gamma-1}{\gamma}M_\infty^2\right]^{\gamma/\gamma-1}-1, \qquad M_\infty \le 1 \tag{4a}$$

$$Cp(0)=\frac{\left[\frac{(\gamma+1)}{2}M_\infty^2\right]^{\gamma/\gamma-1}}{\left[\frac{2\gamma M_\infty^2-(\gamma-1)}{(\gamma+1)}\right]^{1/\gamma-1}}-1, \qquad M_\infty > 1 \tag{4b}$$

The comparison shows good agreement between them. It can be seen from Fig. 4 that the stagnation point pressure coefficient increases with an increase of M_∞.

2.7 Local normal load variations

The probe pressure orifice locations were selected based on local structural load and under no flow separation condition in that region. At each station $Cp(\phi)$ was integrated circumferentially to obtain the aerodynamic load using numerically integrated following relation

$$S\left(\frac{dC_N\alpha}{dx}\right)=2\pi r(x)\int_0^\pi Cp(\phi)\cos\phi d\phi \tag{5}$$

where x is the location of the station from nose, $r(x)$ is radius of cone at station x, ϕ is roll angle from leeward side. $Cp(\phi)$ is a pressure coefficient in circumference direction. C_N is normal force coefficient and S is reference surface areas based on booster diameter d. Local normal forces are computed at various locations using numerically computed circumferential pressure distribution. Fig. 5 shows the local normal force at different sections in the conical region. We have selected x/D=0.77 for mounting pressure transducers as shown in Fig. 1. This location experiences minimum normal pressure load. Fig. 1(b) displays the corresponding flush air data system employed in the estimation of angle of attack and sideslip angle, where subscripts α_1 and α_2 represent windward and leeward of the pitch plane and β_1 and β_2 in the yaw plane as shown in Fig. 1(b).

2.8 Flush air data system calibration

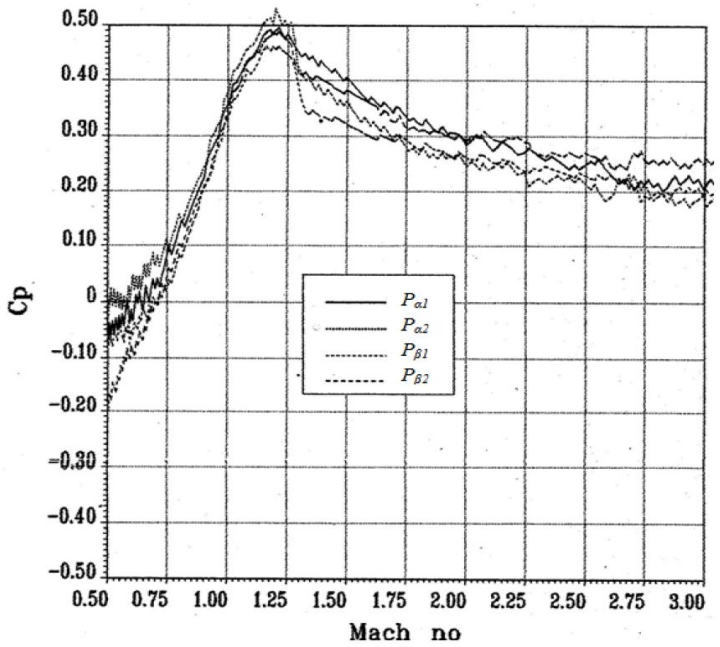

Fig. 6 Measured pressure coefficients vs Mach number at x=0.77 D

Fig. 6 displays the measured pressure coefficients at different ports ($P_{\alpha 1}$, $P_{\alpha 2}$, $P_{\beta 1}$ and $P_{\beta 2}$) at x=0.77 D where x is measured from the stagnation point of the payload fairing. These pressure measurements are used to validate the location of pressure transducers and construct the calibration charts for inverse analysis. In the next section we will describe CRS method in conjunction with neural network technique to estimate pitch, yaw and AoA as a function of flight Mach number.

3. Inverse problem

There is no unique optimization algorithm that solves inverse problem. In dependence on the specific task a global optimization technique has to be selected. Since this information about the system to be optimized is difficult to obtain by a direct search approach, randomized methods are often chosen.

Calibration parameters are derived using the computed and measured differential pressure with small increments of freestream Mach number and AoA. The pitch and yaw angles are calculated from the calculated parameters derived from the numerical simulation of the flowfield over the payload fairing. The calibration factors span the freestream Mach number range of 0.5 to 3.0 which covers maximum dynamic pressure and transonic region of the vehicle. The calibration factors are validated with wind tunnel results and show good agreement between them. Initial results from the ascent air data system are compared with reconstructed trajectory data. The differential pressure transducers are in the range of 13.788×10^3 Pa the pitch and yaw plane differential pressure are linear with respect to the AoA.

The differential pressure, Δp_α and Δp_β, are highly linear with respect to α and β angles, respectively. A CRS method in conjunction with neural network technique is applied to estimate

the AoA from the measured transient differential pressure history during the ascent period of the launch vehicle.

3.1 Differential pressure measurement

The digitization of the flight pressure data is in 256 counts for the full scale range resulting in a data error of 0.41×10^3 Pa for absolute pressure and 0.1096×10^3 Pa for differential pressure. Rosemount model (1984) 1221F2AF of differential pressure transducer of range $17.23\text{-}172.36\times10^3$ Pa (dif) (2.5-25 psid). The sensitive coefficients k_1 and k_2 are 0.6-0.4. Telemetry requirement uses equipment bay (EB) to ground pressures of about 10 Hz response and two power monitoring Fast Fourier Transform (FFT) of pressure data is also needed to filter out unwanted frequencies.

Roll angle relates the orientation of the vehicle relative to the Earth's surface, and does not directly affect surface pressure or aerodynamics. The calibrated differential pressure in pitch and yaw angle are linear functions of AoA. In order to obtain flow direction from these calibration factors, the equations are inverted to get $\alpha=\Delta Cp_\alpha/k_1q_\infty$ and $\beta=\Delta Cp_\beta/k_2q_\infty$ and $\alpha_t=\sqrt{(\alpha^2+\beta^2)}$, where k_1 and k_2 are calibration constant and subscript ∞ represent freestream condition.. The flight data for the FADS were available from the vehicle telemetry system. Fig. 7 shows the measured different pressure versus freestream Mach number. The flight data represents the measured differential pressure in pitch Δp_α and yaw Δp_β planes. The measured differential pressure data was recorded 10 samples per second. In estimation of α and β, one minimizes

$$F(V)=\left|D_C(\Delta\alpha.\Delta\beta)-D_M(\Delta\alpha.\Delta\beta)\right| \tag{6}$$

where D_C and D_M are, respectively, the calculated and measured differential pressure at x= 0.77 D.

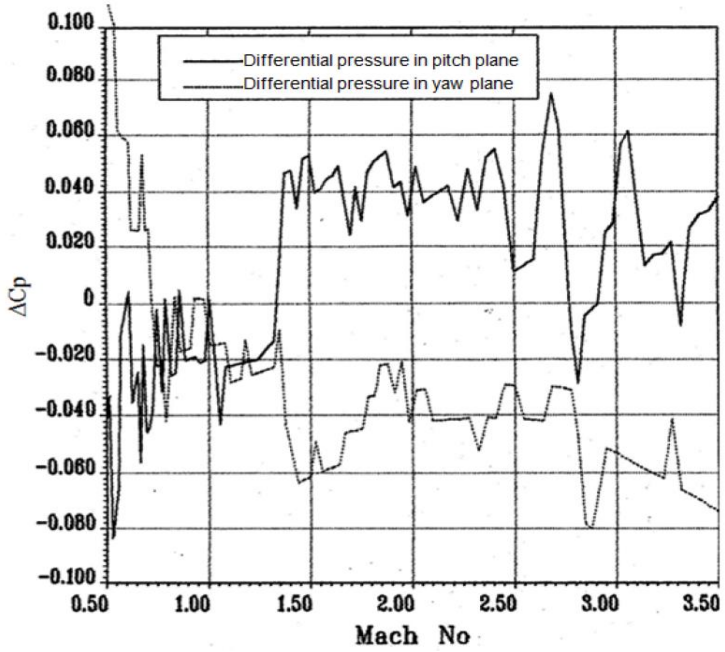

Fig. 7 Measured differential pressure vs Mach number at x=0.77 D

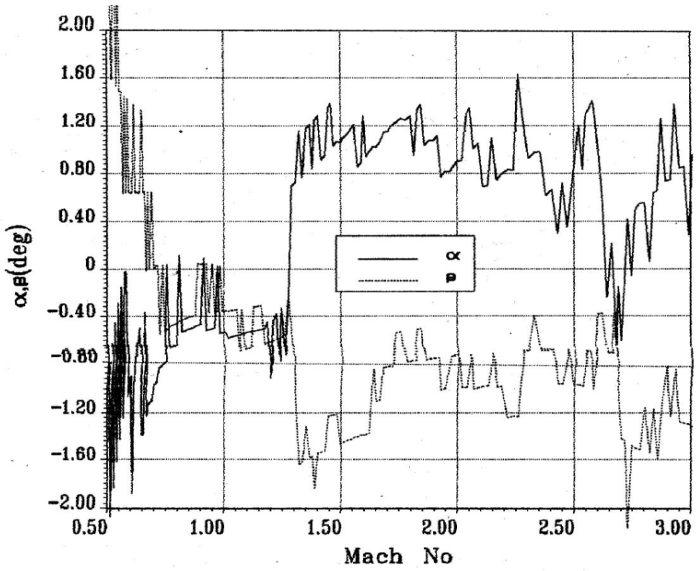

Fig. 8 Estimated values of α and β angle with flight Mach number

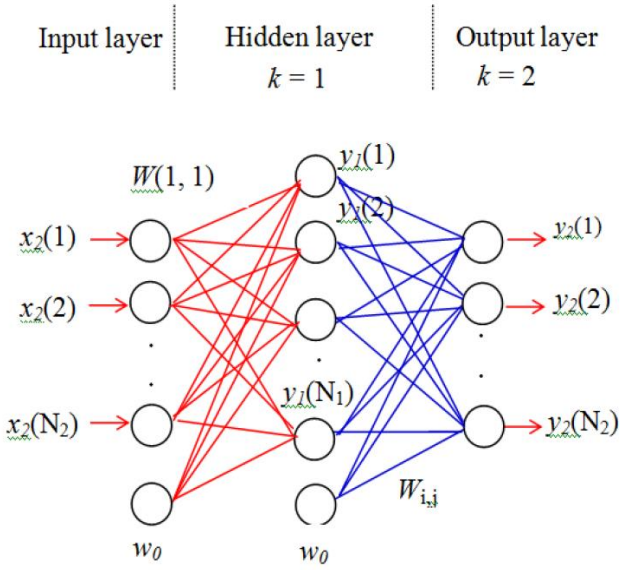

Fig. 9 Topology of multi-layered feed forward neural network

3.2 Controlled random search optimization method

The CRS algorithm (Price 2010), an effective tool for global optimization, does not need computation of derivatives but depends on function $F(V)$ evaluation alone. It works even when the differentiability requirements cannot be assured in the feasible domain of variables. For initiating this algorithm no initial guess value, except for an estimate of V, is needed.

A procedure for solving for α and β unknown air data parameters is now presented. Given that

differential pressure observations are available on the payload fairing. The quantity $F(V)$ is the surface pressure measured by the sensor, and represents the unknown air data parameters which best fit the available set of pressure observations. For differential pressure sensors and solutions require the inversion of an over constrained system.

The CRS algorithm does not need computation of derivatives but depends on function $F(V)$ evaluation alone. The function $F(V)$ is the difference between measured and calculated values of the differential pressure. It works even when the differentiability requirements cannot be assured in the feasible region of the variable. For initiating a CRS algorithm no initial guess value, except for an estimate of α and β is required. The algorithm does not depend on the future-pressure information.

The CRS algorithm is implemented in two steps. In the first step, random feasible points generated from α, β and $F(V)$ are computed at each point and information stored as a matrix. The maximum and minimum values $F_M(V)$, $F_L(V)$ of $F(V)$ and corresponding points M and L are then identified. In the second step, these random points are manipulated iteratively to yield a better candidate for global solutions. To this extent at iteration arbitrary distinct points are selected from the matrix.

The CRS version works in two phases as mentioned by Mehta and Tiwari (2007). In the first phase, random feasibility points generated from V and F are evaluated at each point and the information is stored as matrix A. The maximum and minimum values F_M, F_L of F and the corresponding points M and L are then identified. In the second phase, these random points are manipulated iteratively to yield a better candidate for a global solution. To this extent at iteration arbitrary distinct points are chosen from matrix A. A new point $T=2G-L$, G being the centroid of these points, is generated and if T is in V, then F_T is evaluated. If $F_T < F_M$ then F_M and M in A are replaced by F_T and T. Otherwise, T is discarded and a new T is generated. Treating any replacement as a success and setting the minimum success rate as 0.5, the efficiency of the procedure is enhanced by making use of the secondary trial $Q=(3G-L)/4$. If T or Q is a success, a third trial is also made with $Y=2.5$ (T or Q)-1.5L and the best (with least F value) of T or Q or Y is used for replacement. The iteration process is continued till F_L falls below the prescribed threshold value. The CRS method will be linked with the neural network method in order to get faster convergence of Eq. (6). The convergence criteria are mentioned by Mehta (2017c). It is important to mention here that the CRS and neural network method does not need gradient of the unknown parameters.

3.3 Neural network method

Neural networks (Haykin, 2005), in conjunction with CRS method, is used to estimate angle of attack from differential pressure measurements taken from ports located flush on the blunt-nose of the payload fairing. Fig. 9 exhibits structure of a multi-layered feed forward neural network. Hidden neurons contain weighted connections as input and output. Many input neurons are termed as input layer, hidden neurons as hidden layers and output neurons as output layer. The main task of a neural network is to map input data into output data and to recognize the underlying pattern whereas the data flow is unidirectional from the input layer to the output layer. The mapping from input data to output data is achieved by an adaptation of the network weights. The matrix of weightings of the connections between the neurons can be denoted as the "knowledge" of the network. The error of a neural network may be defined as a least-squares sum between the target values of the training data set and the corresponding network output. During the network training

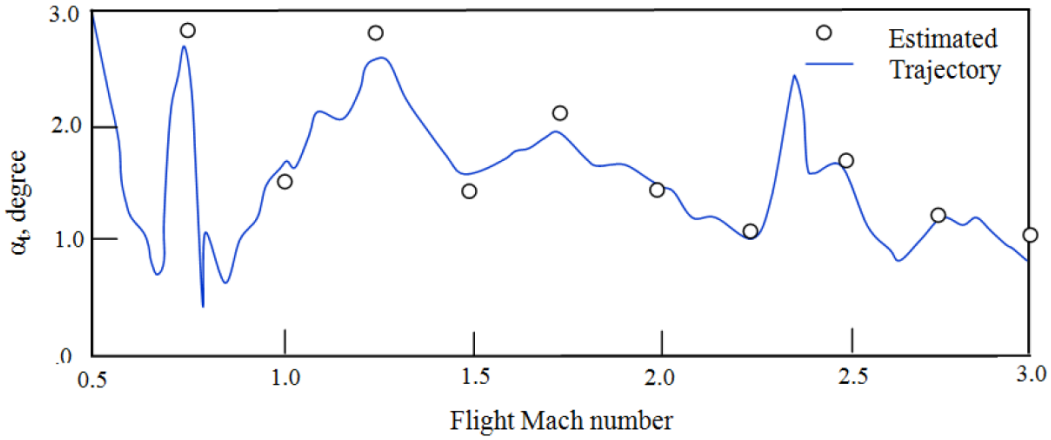

Fig. 10 Comparison of AoA with reconstructed trajectory data

the weighting matrix is adjusted so that the error is minimized.

In order to obtain flow direction from these calibration factors, the equations are inverted to get $\alpha=\Delta Cp_{\alpha}$ and $\beta=\Delta Cp_{\beta}$ and $\alpha_t=\sqrt{(\alpha^2+\beta^2)}$. The results are compared with the reconstructed trajectory data and found in reasonably good agreement.

The further details of CRS algorithm are described in the estimation of discharge coefficient of payload compartment venting by Mehta (2017b). Comparisons of AoA with reconstructed trajectory data are shown in Fig. 10. A good agreement is found between estimated data with reconstructed flight trajectory employing PFA including IMU data.

4. Conclusions

The principal conclusion of this paper is that it is possible to calibrate a flush air data system for a satellite launch vehicle using a computational fluid dynamics approach. Euler calculations have been made to obtain the pressure distributions over the payload fairing in Mach number range of 0.5-3.0. The code employs a three-dimensional finite volume space discretization to solve the integral form of the compressible inviscid equations over the satellite launch vehicle. A CRS method coupled with the neural network technique is employed to estimate the angle of attack and sideslip angle from the measured transient differential pressure history during the ascent period of the launch vehicle. The algorithm predicts the α and β stepwise with the function of Mach number. The predicted values of α and β are found to be consistent with the reconstructed telemetry data as a function of the flight Mach number and found in reasonably good agreement.

References

An, M.Y., Wang, K.C. and Tam L.T. (1993), "Computation of inviscid flow field around 3-D aerospace vehicles and comparison with experimental and flight data", *31st Aerospace Sciences Meeting*, 885. https://doi.org/10.2514/6.1993-885.

Anderson, W., Thomas, J. and van Leer, B. (1986), "A comparison of finite volume flux vector splitting for

the Euler equations", *AIAA J.*, **24**(9), 1453-1460. https://doi.org/10.2514/3.9465.
Baumann, E., Pahle, J.W., Davis, M.C. and White, J.T. (2010), "X-43a flush air data sensing system flight-test results", *J. Spacecraft Rocket.*, **47**(1), 48-61. https://doi.org/10.2514/1.41163.
Bertin, J.J. (2006), *Aerodynamics for Engineers*, 4th Edition, Pearson Education in South Asia, New Delhi.
Chen, G., Chen, B., Li, P., Bai, P. and Ji, C. (2015), "Study on algorithms of flush air data sensing system for hypersonic vehicle", *Procedia Eng.*, **99**, 860-865. https://doi.org/10.1016/j.proeng.2014.12.613.
Cobleigh, B.R., Whitmore, S.A., Haering, Jr., E.A., Borrer, J. and Roback, V.E. (1999), "Flush air data sensing (FADS) system calibration procedures and results for blunt forebodies", *9th International Space Planes and Hypersonic Systems and Technologies Conference*, 4816. https://doi.org/10.2514/6.1999-4816.
Davis, M.C., Pahle, J.W., Marshall, L.A., Mashburn, M.J. and Franks, R. (2000), "Development of a flush air data sensing system on a sharp-nosed vehicle for flight at Mach 3 to 8", *Aerospace Sciences Meeting and Exhibit*, 504. https://doi.org/10.2514/6.2000-504.
Fan, H.Y., Lu, W., Xi., G. and Wang, S. (2003), "An improved neural network based calibration method for aerodynamic pressure probes", *J. Fluid. Eng.*, **125**(1), 113-120 https://doi.org/10.1115/1.1523063.
Haykin, S. (2005), *Neural Networks*, Pearson Prentice Hall, New Delhi, India
Hillje, E.R. and Nelson, R.L. (1983), "Ascent air data system results from the space shuttle flight test program", AIAA Paper, 1980. AIAA-80-0422. https://doi.org/10.2514/6.1981-2457.
Johnston, I.A., Tuttle, S.L., Jacobs, P.A. and Shimoda, T. (1999), "The numerical and experimental simulation of hypervelocity flow around the HYFLEX vehicle forebody", *Shock Wav.*, **9**, 57-67. https://doi.org/10.1007/s001930050139.
Karlgaard, C.D., Kutty, P. and Schoenenberger, M. (2017), "coupled inertial navigation and flush air data sensing algorithm for atmosphere estimation", *J. Spacecraft Rocket.*, **54**(1), 128-140. https://doi.org/10.2514/1.A33331.
Larson, T.J., Moes, T.R. and Siemers III, P.M. (1990), "Wind-tunnel investigation of a flush airdata system at Mach numbers from 0.7 to 1,4", NASA TM 101697, NASA Ames Research Centre California, USA.
Liepmann, H.W. and Roshko, A. (2007), *Elements of Gas Dynamics*, First South Asian Edition, Dover Publications, Inc., printed at Gopsons Papers LTD, Noida, India.
Liou, M.S. (2006), "A sequel to AUSM, Part II: AUSM+-up for all speeds", *J. Comput. Phys.*, **214**(1), 137-170. https://doi.org/10.1016/j.jcp.2005.09.020.
Liu, Y., Xiao, D. and Lu, Y. (2014), "Comparative study on a solving model and algorithm for a flush air data sensing system", *Sensor.*, **14**(5), 9210-9226. https://doi.org/10.3390/s140509210.
Mehta, R.C. (2020a), "Drag reduction for payload fairing of satellite launch vehicle with aerospike in transonic and low supersonic speeds", *Adv. Aircraft Spacecraft Sci.*, **7**(4), 371-385 https://doi.org/10.12989/aas.2020.7.4.371.
Mehta, R.C. (2017b), "Analysis of payload compartment venting of satellite launch vehicle", *Adv. Aircraft Spacecraft Sci.*, **4**(4), 437-448. https://doi.org/10.12989/aas.2017.4.4.437.
Mehta, R.C. (2017c), "Multi-block structured grid generation method for computational fluid dynamics", *Scholar. J. Eng. Technol.*, **5**(8), 387-393. https://doi.org/10.21276/sjet.
Mehta, R.C. and Tiwari, S.B. (2017), "Controlled random search technique for estimation of convective heat transfer coefficient", *Heat Mass Transf.*, **43**(11) 1171-1177. https://doi.org/10.1007/s00231-006-0185-8.
Paces, P., Draxler, K., Hanzal, V., Censky, T. and Vasko, O. (2010), "A combined angle of attack and angle of sideslip smart probe with twin differential sensor modules and doubled output signal", *SENSORS, 2010 IEEE*, 284-289. https://doi.org/10.1109/ICSENS.2010.5689866.
Price, A. (2010), "A controlled random search procedure for global optimization", *Comput. J.*, **26**(4), 367-370. https://doi.org/10.1093/comjnl/20.4.367.
Quindlen, J.F. and Langelaan, J.W. (2013), "Flush air data sensing for soaring-capable UAVs", *51st AIAA Aerospace Sciences Meeting including the New Horizons Forum and Aerospace Exposition*, 1153. https://doi.org/10.2514/6.2013-1153.
Reis, C.J.B., Manzanares-Filho, N. and de Lima, A.M.G. (2019), "Robust optimization of aerodynamic loadings for airfoil inverse designs", *J. Brazil Soc. Mech. Sci. Eng.*, **41**, 207.

https://doi.org/10.1007/s40430-019-1705-z.
Rohlf, D., Brieger, O. and Grohs, T. (2004), "X-31 vector system identification-approach and results", *AIAA Atmospheric Flight Mechanics Conference and Exhibit*, 4830. https://doi.org/10.2514/6.2004-4830.
Rohloff, T.J., Whitmore, S.A. and Catton, I. (1998), "Air data sensing from surface pressure measurements using a neural network method", *AIAA J.*, **36**(11), 2094-2101. https://doi.org/10.2514/2.312.
Rosemount Model (1984), Aerospace Division, Rosemount Inc., Burnsville, Minnesota, USA.
Samy, I., Postlethwaite, I., Gu, D.W. and Green, J. (2010), "Neural-Network-Based flush air data sensing system demonstrated on a Mini Air Vehicle", *J. Aircraft*, **47**(1), 18-31. https://doi.org/10.2514/1.44157.
Shevchenko, A.M. and Shmakov, A.S. (2017), "Multi-hole pressure probes to wind tunnel experiments and air data systems", *AIP Conference Proceedings*, **1893**(1), 030088. https://doi.org/10.1063/1.5007546.
Srivastava, A. and Meade, A.J. (2015), "A comprehensive probabilistic framework to learn air data from surface pressure measurements", *Int. J. Aerosp. Eng.*, 1-19, Article ID 183712. http://doi.org/10.1155/2015/183712.
Watanabe, S., Ishimoto, S. and Yamamoto. Y. (1997), "Aerodynamic characteristics evaluation of hypersonic flight experiment vehicle based on flight data", *J. Spacecraft Rocket.*, **34**(4), 464-470. https://doi.org/10.2514/2.3259.
Whitmore, S.A., Cobleigh, B.R. and Haering, E.A. (1998), "Design and calibration of the X-33 Flush Airdata Sensing (FADS) system", NASA TM 206540, NASA Dryden Flight Research Centre, California, USA.

GY